



# Progressive activation of degradation processes in solid oxide fuel cells stacks: Part I: Lifetime extension by optimisation of the operating conditions

Arata Nakajo<sup>a,\*</sup>, Fabian Mueller<sup>b</sup>, Jacob Brouwer<sup>b</sup>, Jan Van herle<sup>a</sup>, Daniel Favrat<sup>a</sup>

<sup>a</sup> Laboratoire d'Energétique Industrielle (LENI), Institut de Génie Mécanique, Ecole Polytechnique Fédérale de Lausanne, 1015 Lausanne, Switzerland

<sup>b</sup> National Fuel Cell Research Center, University of California, Irvine, CA, United States

## H I G H L I G H T S

- Analysis of the combined effect of multiple degradation processes in SOFC stacks.
- Acceleration of the degradation and sequential activation of processes is predicted.
- Optimisation of the operating conditions can extend lifetime by a factor up to 10.
- Operating conditions for the highest performance and the best durability differ.
- Overpotential rather than current density influences the degradation behaviour.

## A R T I C L E I N F O

### Article history:

Received 1 March 2012

Received in revised form

25 May 2012

Accepted 28 May 2012

Available online 1 June 2012

### Keywords:

Solid oxide fuel cell

Degradation

Repeating unit model

Chromium contamination

Optimisation

## A B S T R A C T

The degradation of solid oxide fuel cells (SOFC) depends on stack and system design and operation. A methodology to evaluate synergistically these aspects to achieve the lowest production cost of electricity has not yet been developed.

A repeating unit model, with as degradation processes the decrease in ionic conductivity of the electrolyte, metallic interconnect corrosion, anode nickel particles coarsening and cathode chromium contamination, is used to investigate the impact of the operating conditions on the lifetime of an SOFC system. It predicts acceleration of the degradation due to the sequential activation of multiple processes. The requirements for the highest system efficiency at start and at long-term differ. Among the selected degradation processes, those on the cathode side here dominate. Simulations suggest that operation at lower system specific power and higher stack temperature can extend the lifetime by a factor up to 10, because the beneficial decrease in cathode overpotential prevails over the higher release of volatile chromium species, faster metallic interconnect corrosion and higher thermodynamic risks of zirconate formation, for maximum SRU temperature below 1150 K. The counter-flow configuration, combined with the beneficial effect of internal reforming on lowering the parasitic air blower consumption, similarly yields longer lifetime than co-flow.

© 2012 Elsevier B.V. All rights reserved.

## 1. Introduction

Distributed power generation is a foreseen application for solid oxide fuel cell (SOFC) devices. Combined heat and power systems, even small ones, based on this technology could achieve high efficiencies, fuel flexibility and load following capabilities along with low maintenance costs and noise nuisance. Despite many advances, SOFC prototypes do not yet meet the reliability and durability standards of the industry. Unresolved structural issues

affect the reliability by hindering a completely safe assembly and operation of the cells, whereas the degradation of the electrochemical performance limits the durability.

SOFC system design and operation must aim at the lowest achievable cost of electricity under practical conditions that support utility grid operation, as well as end-user and owner demands [1]. To appropriately meet these requirements, they have to be integrated with lifetime analysis, since they are known to have a strong impact on the SOFC degradation [2,3]. Because of the various underlying physical phenomena, this involves to retrieve knowledge from different research fields and length scales. To our knowledge, an integrated methodology to evaluate stack and system design and operation in the view of electrochemical and

\* Corresponding author. Tel.: +41 21 693 35 05.

E-mail addresses: [arata.nakajo@uconn.edu](mailto:arata.nakajo@uconn.edu), [arata.nakajo@epfl.ch](mailto:arata.nakajo@epfl.ch) (A. Nakajo).

mechanical degradation has not yet been developed. Such a tool could help to further approach the potential capabilities of the SOFC technology [4,5].

Button cell endurance tests in inert alumina test arrangements exhibit degradation, induced by localised microstructural alterations of the materials and interfaces of the membrane electrode assembly (MEA), due to particle coarsening [6–11], detrimental reactions between the materials [12–14] or impurities in the starting powders [15]. In an SOFC stack, the cost-effective interconnects, sealants and gas diffusion layers (GDL) amplify material incompatibilities, hence the degradation, because of their lower stability than the MEA materials in the SOFC environment [16]. The transport of contaminants by the gases increases the distance over which detrimental interactions operate [17]. The uneven distributions of temperature, current density, gas composition and overpotential in a stack, induce different local degradation rates. The interactions between the detrimental processes govern their evolutions, which accounts for a progressive acceleration of the degradation rate [18]. An efficient mitigation strategy must determine a suitable nominal operating point that balances power density and efficiency requirements with lifetime. Spatial temperature control can alleviate the progressive accumulation of damage under comparatively more harmful operation during load following, which can affect the durability of the SOFC stack [19].

Owing to the multiphysics nature of degradation, models are of interest to first improve the relevance and efficiency of the development cycles, and then to adjust the product for each application. The mitigation of degradation through improvements of the stability of the MEA and other single repeating unit (SRU) components is in progress and controversy remains. As discussed in Ref. [20], because the focus of experimental studies is principally on either (i) gaining knowledge on the underlying processes or (ii) scanning for the best technological solution, the range of investigated conditions does usually not cover that found in SOFC stacks in operation. Herein lies their partial incompatibility, in particular that of (ii), with modelling at the SRU/stack scale. The range of operation is determined by indicators for anode reoxidation [21] or cathode reduction in the case of imperfect sealants [22,23]. The SRU geometry and gas manifold is adjusted to reduce high local current densities to avoid ensuing high localised rates of heat generation and current constriction effects. More refined analyses [24] seek to identify the patterns of degradation in electrochemical impedance spectra (EIS) for in-operation diagnostics. The next step is to implement the multi-factorial and history-dependent nature of SOFC degradation in SRU models, for reliable lifetime predictions and integrated mitigation approaches. The state-of-the-art understanding of the SOFC degradation is not precise enough to support the completion of this difficult aim. It however provides a starting point that can serve, in synergy with experimental tasks, to gain knowledge on the underlying physics and must be accordingly and continuously updated.

In this study, a simulation tool has been developed to support stack design and operation in the view of both lifetime and electrical efficiency. Our calibrated electrochemical model, which includes several simultaneous degradation phenomena [20,25] is implemented in SRU models of a planar, intermediate-temperature, anode-supported stack design to investigate their combined detrimental effect on the durability under the practical operating conditions an SOFC stack must withstand in the field. The decrease in ionic conductivity of 8YSZ, metallic interconnect (MIC) corrosion, nickel particle growth and chromium contamination of the LSM–YSZ cathode, completed by transport of volatile chromium species [22], are considered. This Part I investigates the effects of operating conditions on the start-up and long-term performance of SOFC stacks, to identify the potential of this practical approach to extend the lifetime and assist the exploration of the operating

envelope of SOFC devices. Part II [26] focuses on the distribution of the degradation over the active area. System considerations are restricted to the parasitic loss of the air blower and efficiency of the inverter, to avoid the computational burden of a complete integrated system model, yet capture the key system efficiency characteristics. Operating conditions are optimised for co-flow and counter-flow configurations, along the trade-off between system power and efficiency, first for the best initial, then for the best long-term electrical efficiency during operation at a fixed system power, to verify whether both cases generate similar requirements or not. The methane conversion fraction in the reformer and the allowable maximum solids temperature are handled as discrete decision variables, for further structural analysis [27,28], as these are believed to significantly affect the thermomechanical behaviour of the SRU. The lifetime predictions during operation at constant system power are compared with those at fixed current density, voltage or stack power, which are more common in stack testing.

## 2. Modelling approach

This study uses a one-dimensional modular model of an SRU implemented in gPROMS [29], an equation-oriented process modelling tool. Thermal boundary conditions are imposed to represent the conditions in an SRU embedded in a stack. The detailed description is provided in Ref. [25]. The framework is the

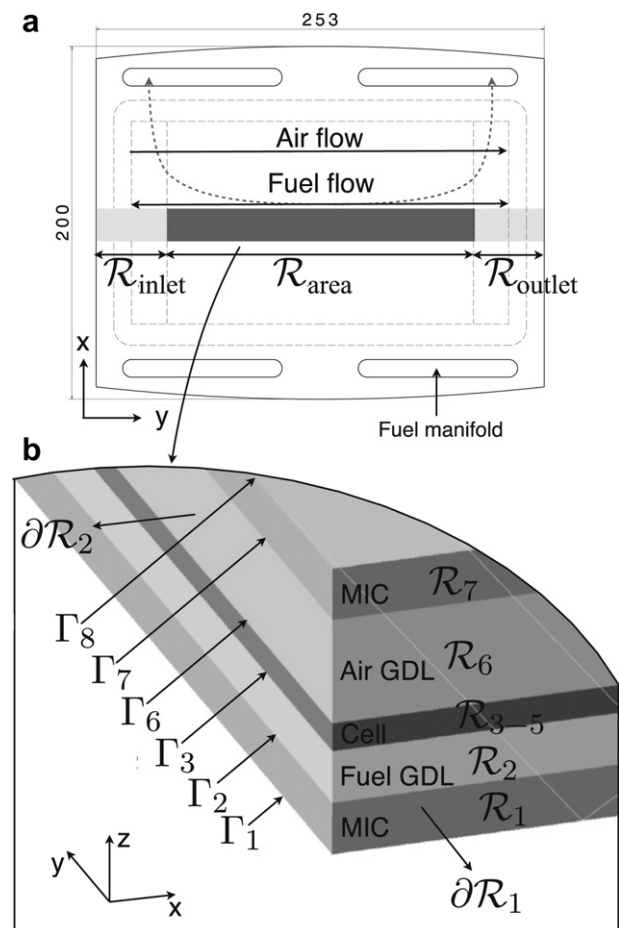


**Fig. 1.** (a) View of the FlameSOFC SRU design and one-dimensional simplification for the calculations. (b) Description of domains and boundaries in the model [25].  $R$ : domains,  $\Gamma$ : interfacial boundaries,  $\partial R$ : boundaries, GDL: gas diffusion layer, MIC: metallic interconnect, area: active area, inlet/outlet: gas manifold zones.

design developed within the FP6 European FlameSOFC project. Its objective was the development of a 2.5 kWe SOFC stack for combined heat and power (CHP) application. In the project, fuel processing was based on thermal partial oxidation. Here, steam–methane reforming is considered in addition, because of the higher achievable efficiencies. Fig. 1 depicts the actual geometry, along with the computational domains of the one-dimensional model.

The electrochemical model considers both ohmic and non-ohmic losses. The description and calibration of the parameters on experimental data from two different segmented-cell tests was provided elsewhere [25]. The main features are recalled hereafter.

- Ohmic losses comprise the ionic resistivity of the electrolyte, corrected for constriction effects; the electronic resistivity of the MIC, its oxide layer and contact resistance; and a limited electronic conductivity of the electrolyte that induces a small leakage current.
- On the cathode side, a specific modelling approach is needed for either an LSM–YSZ or else lanthanum strontium cobaltite ferrite (LSCF) cathode. In this study, the focus is on LSM–YSZ cathode. A model of composite electrode solves the charge balance along with mass transport. The transfer current is computed following the sequence of elementary processes proposed by van Heuveln et al. [30], adapted for a low coverage of adsorbed oxygen species. The performance of the LSM–YSZ cathode on which the electrochemical model had been previously calibrated [25], is significantly lower than today's state-of-the-art. For instance, the cell potential at 1073 K and  $0.3\text{--}0.7\text{ A cm}^{-2}$  is approximately 10–50 mV lower than that reported by de Haart et al. [18]. This results in efficiencies lower than expected and shorter lifetime, but does not preclude the analysis. The case of LSCF cathode has been considered for comparison. Here, the modelling approach follows that proposed by Adler et al. [31]. Experimental data from the literature are used to compute the dependence of the equilibrium vacancy concentration on temperature and oxygen partial pressure and surface exchange properties at the pore wall. Direct exchange of vacancies with the electrolyte is assumed [32].
- On the anode side, the dusty-gas model is solved in one-dimension, through the thickness of the support, along with the equation of continuity. The steam-methane reforming rate is computed by the kinetic approach of Achenbach and Riesenche [33] and the water–gas shift reaction is assumed at equilibrium in the anode. Only hydrogen is electrochemically converted at the interface, following the set of elementary processes proposed by Zhu et al. [34].

This electrochemical model based on physical principles is compatible with the implementation of degradation phenomena. The description of the modelling approach, the value of the parameters and the analysis of the local behaviour can be found in Ref. [20]. The selected degradation phenomena are the (i) decrease in ionic conductivity of 8YSZ, (ii) MIC corrosion, (iii) anode nickel particle growth and, (iv) chromium contamination and (v) formation of zirconates in the LSM–YSZ cathode. The main features of the degradation models are summarised as follows:

- A classical percolation model predicts the reduction of the triple-phase boundary (TPB) due to the growth of nickel particles in the anode. The semi-empirical relation for the evolution of the nickel particle radius depends on temperature, steam and hydrogen partial pressure and tends to a maximum value due to the mechanical constraint imposed by the YSZ network. In the model, the time to reach the plateau value spans from 1000 h to 10,000 h [20] under the local conditions found in an intermediate SOFC stack.

- An empirical model reproduces the experimental data on the decrease of the ionic conductivity of 8YSZ samples during ageing in air. The temperature-dependent plateau value is reached in the model after 500 h–2500 h [20]. The trend in the evolution after ageing during more than 5000 h is not included in the data. Errors may arise from extrapolation. This degradation process affects both the electrolyte and the 8YSZ phase in the LSM–YSZ cathode. Recovery of the ionic conductivity is not allowed.
- The maximum SRU temperature in intermediate-temperature SOFC is limited, among others, by the oxidation resistance and high-temperature mechanical properties of the metallic components. This is not included in the present study, because a consistent set of data on the temperature dependence of the evolution of the area specific resistance (ASR) of coated MIC could not be found. The relation by Liu et al. [35] for the growth of the oxide scale under a  $\text{Mn}_{1.5}\text{Co}_{1.5}\text{O}_4$  coating that is used in the present study is valid at 1073 K exclusively.
- The modelling of chromium contamination of LSM–YSZ cathode assumes the progressive blocking of the active sites by the electrochemical deposition of  $\text{Cr}_2\text{O}_3$  from  $\text{CrO}_2(\text{OH})_2$  (g) released by the MIC and upstream system metallic components. This process depends upon the steam and  $\text{CrO}_2(\text{OH})_2$  (g) partial pressures and assigned to the local overpotential within the composite cathode. Many other volatile species can be involved [36–39]. For consistency, a small amount of steam is needed in the air. The value of 0.1% used here is typical for compressed air, commonly used in stack tests [40]. It should be emphasised that depending on the humidity, other phenomena, not necessarily related to chromium contamination, may predominantly cause the degradation of the LSM–YSZ cathode [41]. Chromium contamination and air humidity affect LSCF and lanthanum strontium ferrite cathodes as well, but the degradation mechanisms differ [41–43]. This restricts the use of the chromium contamination modelling approach developed here to LSM–YSZ.
- Indicators are used for the risk of reoxidation of the anode [21] and formation of undesirable zirconate phases (LZO, SZO) in the LSM–YSZ cathode. For the latter, the thermodynamic data on the critical oxygen partial pressure from Liu et al. [12] is interpolated and compared with the local one, computed from the local overpotential and oxygen gas phase concentration.

Degradation analysis under practical operating conditions requires the calculation of the transport of volatile chromium species on the air side and SOFC system considerations.

## 2.1. System considerations

The aim of the implementation of system considerations is to capture the essential implications of system integration on the operation of the SOFC stack, while keeping the additional computational load as low as possible and avoiding the complexity of an

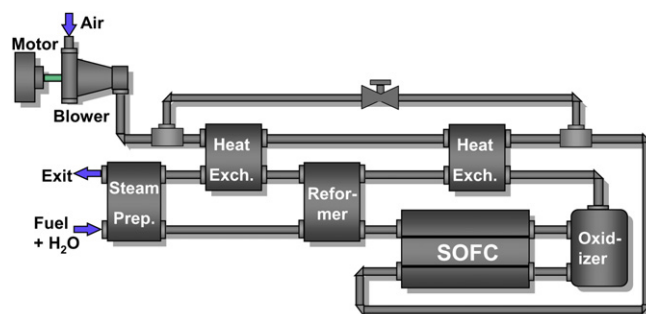


Fig. 2. Schematic view of a typical layout of SOFC system for CHP application.

**Table 1**  
Thickness of the MEA and SRU components.

	Electrolyte	Compatibility layer <sup>a</sup>	Cathode	Anode	GDL <sub>a</sub>	GDL <sub>c</sub>	MIC
Material	8YSZ	20GDC	LSCF LSM–YSZ	Ni-8YSZ	Ni foam	Crofer22APU <sup>b</sup> foam	Crofer22APU <sup>b</sup>
h (m)	7e-6	7e-6	60e-6	540e-6	1e-3	2e-3	2e-3

<sup>a</sup> Implemented in the case of LSCF cathode.

<sup>b</sup> Commercial denomination, of ferritic alloy [62].

extensive system integration study. Fig. 2 shows a schematic view of a system layout for CHP application. Previous analyses using this system configuration [44] have demonstrated a large system operating envelope with sufficient heat integration for air pre-heating and variation of the methane conversion fraction within the reformer in the range of conditions considered here. Assuming the system is well thermally integrated as has been shown in prior work [44], the dominant system auxiliary losses that dictate system performance are those due to the air blower and inverter.

The power consumption of the air blower per SRU in the stack is computed using isentropic relations [44]. The isentropic efficiency is 0.8.

$$P_{blwr} = \dot{N}_{air} \frac{1}{\epsilon_{blwr}^{eff}} \frac{\gamma}{\gamma - 1} RT_{amb} \left[ \left( \frac{p_{sysout}}{p_{atm}} \right)^{\frac{\gamma}{\gamma - 1}} - 1 \right] \quad (1)$$

The calculation of the stack pressure drop on the air side is based on empirical relations for the permeability of metallic foams [45]:

$$B_o = 8 \cdot 10^{-15} \exp(16.39n) \quad (2)$$

A simple linear approximation is used for the dependence on temperature of the air viscosity, between 950 K and 1150 K [46]. The variation of composition along the channel is neglected, because of the high air ratio:

$$\frac{\partial p}{\partial y} = -\frac{\mu_{air}}{B_o} u_{air} \text{ in } \mathcal{R}_6, \text{ over } \mathcal{R}_{inlet}, \mathcal{R}_{area}, \mathcal{R}_{outlet} \quad (3)$$

As a study case, the pressure drop in the heat exchanger network in Fig. 2, needed for air pre-heating and fuel processing, is assumed to be twice that of the stack. The definition of the specific system power is based on the SRU active area, a constant inverter efficiency of 93% and methane fed in the system.

$$\mathcal{P}_{sys} = \frac{\epsilon_{inv}^{eff} P_{SRU} - P_{blwr}}{A_{\mathcal{R}_{area}}} \quad (4)$$

$$\epsilon_{sys}^{eff} = \frac{\epsilon_{inv}^{eff} P_{SRU} - P_{blwr}}{\dot{N}_{CH_4} LHV_{CH_4}} \quad (5)$$

**Table 2**  
Objectives, values of the discrete decision variables and range of the continuous decision variables in the optimisation problems.

Objective	
System efficiency ( $\epsilon_{sys}^{eff}$ )	
System specific power ( $\mathcal{P}_{sys}$ ) <sup>a</sup> (W cm <sup>-2</sup> )	0.18; 0.35
Time (h)	2000
Discrete decision variables	
Max. SRU temperature (K)	1100; 1125; 1150
Reformer conversion fraction	0.25; 0.50; 0.75; 0.99
Continuous decision variables <sup>b</sup>	
Fuel utilisation	0.6–0.95
Air inlet temperature (K)	600–1080

<sup>a</sup> Second objective; sequentially varied (see text).

<sup>b</sup> Interval for optimisation.

## 2.2. Transport of chromium volatile species

At the SRU level, a gas-tight sealing solution yields a uniform steam partial pressure on the cathode side. In contrast, the content of  $\text{CrO}_2(\text{OH})_2$  released by the MIC is governed by mass transport limitations, as suggested by Opila et al. [47]. Except for the deposition process (see Ref. [20]), the present approach follows that proposed by Wuillemin [22], the main features of which are recalled here.

The partial pressure of  $\text{CrO}_2(\text{OH})_2$  over the oxide scale of the MIC is assumed at equilibrium and computed from thermodynamic data for  $\text{Cr}_2\text{O}_3$  [48,49]:

$$\log K_{\text{CrO}_2(\text{OH})_2}^{eq} = -2978 \cdot T_s^{-1} - 1.96 \quad (6)$$

$$x_{\text{CrO}_2(\text{OH})_2} = K_{\text{CrO}_2(\text{OH})_2}^{eq} \cdot x_{\text{H}_2\text{O}} \cdot x_{\text{O}_2}^{3/4} \quad (7)$$

In the fully developed region of a laminar flow, the analogy between heat and mass transport, i.e.  $\text{Nu} \cdot \text{Pr}^{-1/3} = \text{Sh} \cdot \text{Sc}^{-1/3}$  [46], simplifies the one-dimensional mass conservation equation of  $\text{CrO}_2(\text{OH})_2$ :

$$u_{air} \frac{p_{atm}}{RT_g} \frac{\partial x_{\text{CrO}_2(\text{OH})_2}}{\partial y} = \mathfrak{R}_{\text{CrO}_2(\text{OH})_2}^{vap} + \mathfrak{R}_{\text{CrO}_2(\text{OH})_2}^{dep} \quad (8)$$

$$\mathfrak{R}_{\text{CrO}_2(\text{OH})_2}^{vap} = -\frac{1}{h_{air}} \left[ \frac{p_{atm}}{RT} \frac{\text{Nu} D_{\text{CrO}_2(\text{OH})_2}^e}{L} (x_{\text{CrO}_2(\text{OH})_2} - x_{\text{CrO}_2(\text{OH})_2}^{eq}) \right] \quad (9)$$

$$\mathfrak{R}_{\text{CrO}_2(\text{OH})_2}^{dep} = -\frac{1}{h_{air}} \frac{i_{o_{cath}} x_{\text{CrO}_2(\text{OH})_2}^{1/2} x_{\text{H}_2\text{O}}^{1/2}}{A_{\mathcal{R}_{area}} F} \int_{z=0}^{z=h_{cath}} \mathcal{V}_{cath}(z) A_{TPB}(z) 2 \sin h \left( \frac{1}{2} \frac{F \eta_{cath}(z)}{RT_s} \right) dz \quad (10)$$

As a first approximation,  $D_{\text{CrO}_2(\text{OH})_2}^e = 2.25 \cdot 10^{-5} \text{ m}^2 \text{ s}^{-1}$  [22].

This approach significantly simplifies the real situation in an SOFC stack:

- In ferritic alloys for SOFC application, a  $(\text{Mn,Cr})_3\text{O}_4$  spinel develops on top of the oxide scale [50]. It alleviates the release of chromium species, due to the thermodynamic equilibrium, as shown by computations for  $\text{MnCr}_2\text{O}_4$  in humid air [51]. The situation is further complicated in a coated MIC. The use of thermodynamic data for the equilibrium partial pressure of  $\text{CrO}_2(\text{OH})_2$  over  $\text{Cr}_2\text{O}_3$  therefore yields conservative lifetime predictions, even though the scatter in the thermodynamic data induces imprecision in the range of one order of magnitude [22,47,51].
- Resistance against mass transport of  $\text{CrO}_2(\text{OH})_2$  from the air channel to the active sites where it is electrochemically deposited, is neglected. This assumption is conservative, but prevents the use of the model for reliable guidance in the choice of the



cathode thickness or microstructure or current collector materials that may act as a contamination-protecting layer.

The present modelling approach partially captures the complexity of SOFC degradation, because the underlying physics is highly dependent on the materials and conditions and the understanding is in progress. It however reproduces the correct trends, without any specific adjustment [20], but cannot comply with all the observations from post-mortem analyses [18,52,53] under any tested conditions. For such an achievement, the number of implemented degradation mechanisms and the level of refinement in their description must be increased, which requires in future a more intricate interrelationship between experiments and modelling. We believe, for example, that for the relevance of the chromium contamination model, the most critical limitations arise from the lack of knowledge on the deposition process, and insufficient data to determine, even imperfectly and empirically, the temperature dependence of the process.

### 3. Investigated cases

Apart from costs and application-related considerations, the end-user specifies the electrical power output of the SOFC system that must be delivered at the highest efficiency and power density. The target electrical power of a given SOFC device can be achieved by manipulating various sets of operating parameters. A sensitivity analysis on the influence of each single parameter on the initial and long-term performance generates a large amount of data, the analysis of which may not clearly highlight the key dependences. The formulation of an optimisation problem can reduce the complexity and amount of simulations needed for a useful analysis.

This study uses the simple sequential approach for multi-objective optimisation applied in the SOFC field by Larrain et al. [54]. The procedure consists in performing optimisations on one objective, the other being subjected to a constraint that is sequentially modified to cover the desired range of variation. A second run, where the effective and constrained objectives are switched, should be performed for improved reliability. Computing time is spared here for extended variations in the decision variables, rather than for a second optimisation run, since the focus is on the identification of trends, not on the effectiveness of the multi-objective optimisation method.

Optimisations with the system specific power and efficiency as conflicting objectives are carried out separately for the co-flow (CO) and counter-flow (COU) configurations.

The case of highest system efficiency at start is first investigated. An ideal multi-objective optimisation includes all decision variables to provide directly design guidelines. In reality, both thermo-electrochemical and structural issues govern the reliability and durability of SOFC devices. Thermo-electrochemical aspects are included in the one-dimensional model, to the limit of the refinement of the model (see Section 2 and Refs. [20,25]). The lack of knowledge on mechanical failures in SOFC stacks, and the variety of their nature, prevent their simplification to indicators, hence simple implementation in the optimisation problem. For future structural analysis [27,28], discrete values of the decision variables that mainly govern the temperature profile in an SRU embedded in a stack are enforced, within the typical range for intermediate-temperature, anode-supported SOFCs:

- The maximum allowable SRU solids temperature range considered here (1100 K, 1125 K or 1150 K) influences the relative contribution of residual and thermal stresses in the different components of an SRU, as well as the creep and rate-independent plastic behaviour of the materials [55].

- The variation of the methane conversion fraction in the reformer (25%, 50%, 75% or 99%) affects the magnitude, position and extent of zones of localised higher temperature that induce detrimental stresses in the SRU components. The steam-to-carbon ratio is two for all cases.

The control of the maximum SRU temperature assumes a proper instrumentation (direct or not) of the stack which is needed if spatial temperature control is foreseen [19]. The air inlet temperature determines the air ratio and influences the temperature difference over the SRU. On the fuel side, the fuel utilisation sets the fuel flow. The fuel inlet temperature is maintained at 973 K in all cases. Table 1 lists the thicknesses of the components that are identical to those in Ref. [20]. Table 2 summarises the objectives and decision variables.

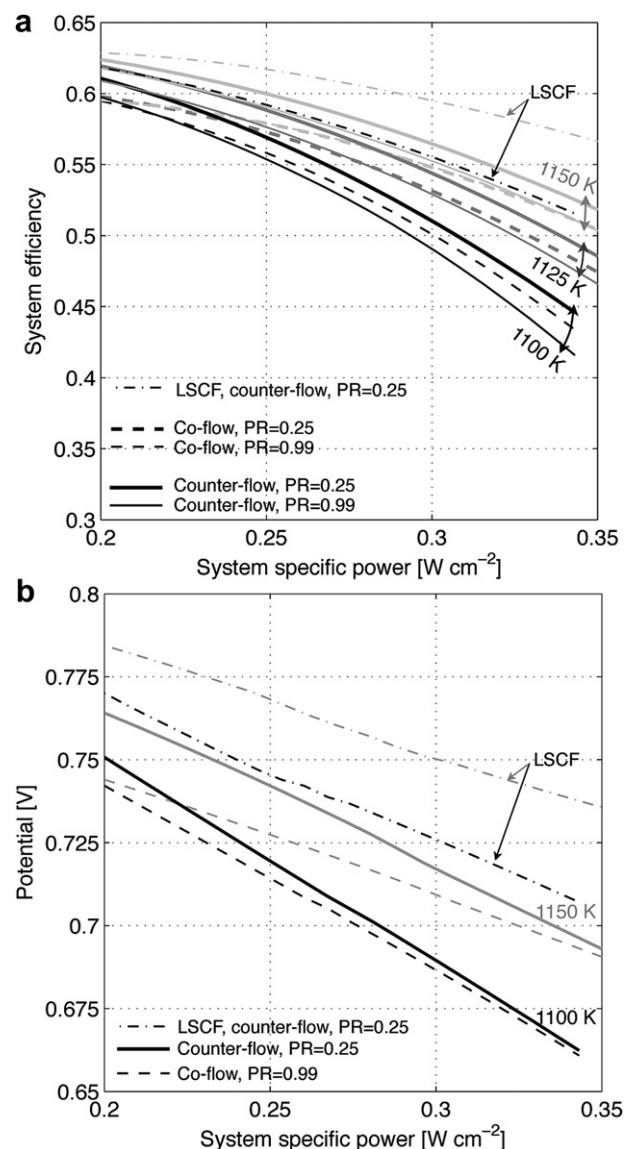


**Fig. 3.** (a) Optimised initial system efficiency (Eq. (5)) and (b) SRU potential vs. specific system power, for the co-flow (dashed lines) or counter-flow (solid lines) configurations, with a fixed maximum allowable cell temperature of 1100 K, 1125 K or 1150 K (black to light grey), and methane reforming fraction in the reformer (PR) of 0.25 (thick lines) or 0.99 (thin lines). Optimisation results for LSCF cathode are provided for comparison (markers, 1100 K, 1150 K, PR = 0.25 and counter-flow).

For the case of the highest system efficiency at long-term, a dynamic optimisation procedure, where the time dependence arises from the degradation phenomena in the model, is performed using the same objectives and decision variables as for the steady-state optimisation procedure (Table 2). The value of all decision variables, equivalently control variables, is kept constant during the whole ageing period. Indeed, in the absence of a refined control, a fixed maximum SRU temperature and air inlet temperature prevent a drastic modification of the temperature profile, whereas a fixed fuel utilisation limits the risk of anode reoxidation. The optimisations are not subjected to end constraints on the risk of formation of LZO/SZO and anode reoxidation. These indicators are monitored for analysis.

The time horizon influences which degradation phenomena are predominantly alleviated by the dynamic optimisations. A lifetime criterion is not straightforward to select and to implement in the optimisation problem. A fixed time horizon represents an owner lifetime requirement. In the present conditions, a value of 2000 h is short enough to avoid numerical failures in the high system specific power regime, yet sufficient to capture longer-term characteristics, since the degradation of the ionic conductivity of 8YSZ and of the anode due to nickel particle growth are close to their plateau at this time [20]. Fixed gas channel geometry, rather than constant system pressure is enforced, as the focus is on the operating conditions rather than on SRU design, and for consistency with structural analysis [27,28].

The effect of operation type and system pressure drop on the degradation is investigated for the operating conditions for the

highest electrical efficiency at long-term and system specific power of  $0.25 \text{ W cm}^{-2}$ . Three scenarios are compared: (i) constant current, (ii) constant SRU voltage and (iii) constant system specific power. The third operation mode results in the highest current levels as degradation lowers the voltage. This accelerates degradation, predominantly that of the cathode due to Cr contamination (see Section 4.2), faster than (i) and (ii).

Multi-objective optimisation results commonly exhibit some scatter, when plotting the optimised decision variables against one of the objectives [56,57]. For clarity, the figures that provide the optimal values of the decision variables, temperature difference and SRU potential, as a function of the system specific power use trend lines instead of actual data. The maximum error is provided for indication and could be likely reduced by a second optimisation pass.

## 4. Results and discussion

### 4.1. Optimisation of the system electrical efficiency at start

Fig. 3 depicts the trade-off between system efficiency and system specific power at start, and corresponding SRU potentials. The difference between the trend line and the actual data is in the worst case less than 1% and 3% for the efficiency and potential, respectively. Fig. 4 depicts the optimal values of the continuous decision variables and the temperature difference in the SRU. The efficiencies fall within the range reported for micro-CHP devices running on natural

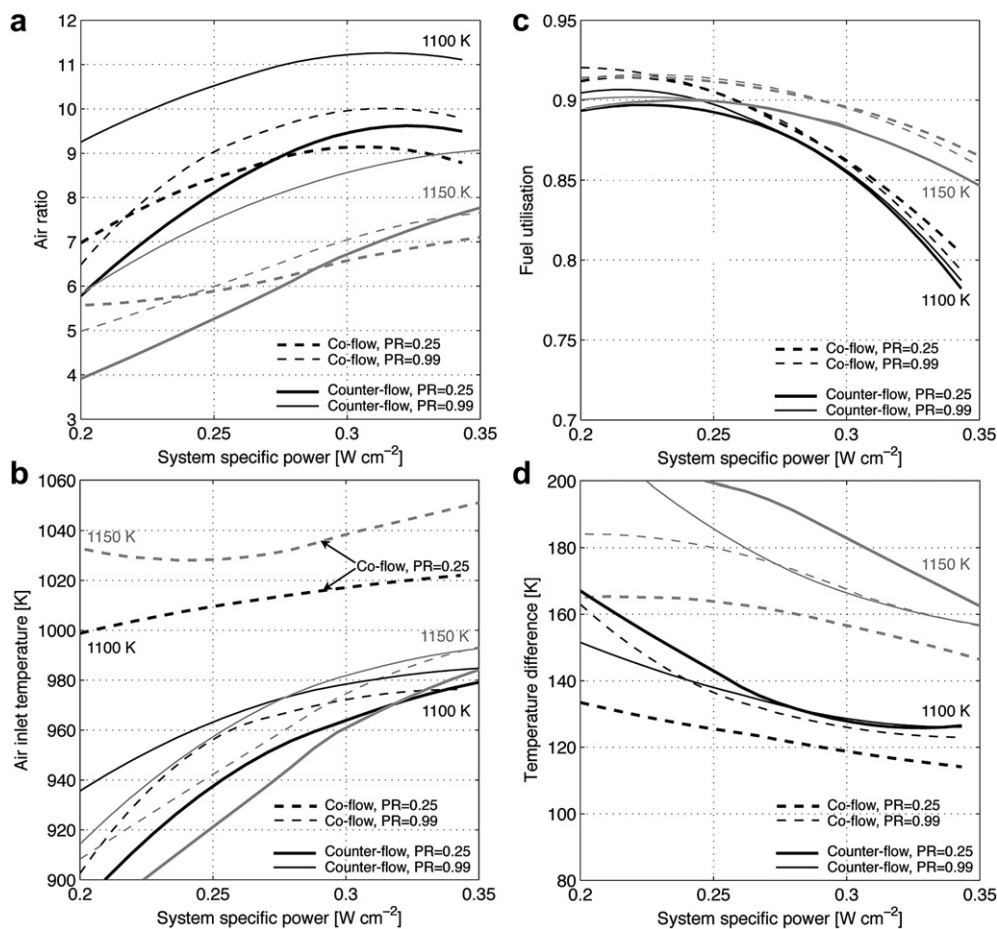


**Fig. 4.** Operating conditions to achieve the highest system efficiency at start depicted in Fig. 3: (a) air ratio, (b) stack air inlet temperature, (c) fuel utilisation, and (d) resulting temperature difference over the SRU, for the co-flow (dashed lines) and counter-flow configuration (solid lines), with a fixed maximum allowable cell temperature of 1100 K (black) and 1150 K (light grey), and methane conversion fractions in the reformer of 0.25 (thick lines) and 0.99 (thin line). The largest discrepancy between the trend line and actual results is 13% (air ratio).

gas. The specific power of the SRU, i.e. without the parasitic power consumptions of the air blower and inverter, and the average current density, ranges from 0.22 to 0.41 W cm<sup>-2</sup> and 0.29 to 0.64 A cm<sup>-2</sup>, respectively. Because of the conservative performance of the considered LSM–YSZ cathode, the SRU potential is low for this technological solution. For comparison, the LSCF cathode yields a significant improvement in both system efficiency and SRU potential. Among the discrete decision variables, the maximum SRU solids temperature predominantly influences the system efficiency. Despite the low SRU potentials and high fuel utilisation, anode reoxidation affects none of the optimisation results.

The gain in system efficiency due to a decrease of the system specific power is less significant at low system specific power. The display is restricted to a value of 0.2 W cm<sup>-2</sup> because of the effect of the leakage current in the electrolyte, which induces a decrease of the system efficiency starting around 0.18 W cm<sup>-2</sup>. This phenomenon has been implemented because in the data used for the model calibration, open-circuit voltages slightly lower than expected were measured [25]. This has been previously tentatively ascribed to an increase of the ionic conductivity of the thin YSZ electrolyte because of undesirable doping during the cell production [21]. Such phenomenon has not been observed in our tests of more recent cells, for which sufficient experimental data for model calibration is however currently not available. The simplified modelling approach of this phenomenon hinders a detailed and reliable analysis. Owing to the high electronic ASR of the electrolyte (50 Ω cm<sup>2</sup>), the leakage current density is lower than 15 mA cm<sup>-2</sup> in most cases, which results in a decrease of the system efficiency of 1–2% in the range displayed in Fig. 3. Compressive gasket materials are not completely impervious [58] and may induce a similar trend with however a different temperature dependence.

The relationship between the potential and specific system power follows a linear trend (Fig. 3). In contrast, the more pronounced decrease of the system efficiency at high specific system power is due to that of the fuel utilisation, which must be lowered for increased current density, because diffusion limitations issues in the thick anode support become more significant. The relative parasitic consumption of the air blower further amplifies this trend.

#### 4.1.1. Discrete decision variables

The required air ratio to maintain the SRU maximum temperature within specified limits is high (see Fig. 4). At a first sight, internal reforming can reduce it and therefore yield a benefit on the system efficiency. The effect of methane conversion fraction in the reformer depends on the flow configuration, as shown in Fig. 3. It barely influences the system efficiency in co-flow, whereas internal reforming (PR = 0.25) is beneficial in counter-flow. Fig. 5 qualitatively depicts the effect of methane conversion fraction in the reformer on the temperature and current density profile in co- and counter-flow configuration. In co-flow, the location of the maximum current density follows a trade-off between high temperature and lean fuel mixture. At high fuel utilisation, it is located close to the fuel inlet side of the active area, which is the zone cooled by the endothermic steam–methane reforming reaction. Therefore, the air inlet temperature is comparatively increased, as shown by Fig. 4b, to avoid a very low electrochemical performance in this area, at the cost of a higher air ratio, hence air blower parasitic consumption. The effect of internal reforming on the system efficiency is therefore marginal in co-flow. In contrast, it is beneficial for the system efficiency in the counter-flow configuration, because the cooling effect of the steam–methane reforming reaction acts close to the zone of highest temperature, i.e. air outlet side of the active area. A higher air inlet temperature is therefore not needed, which enables a significant decrease of the air ratio, and consequently an increase of the system efficiency.

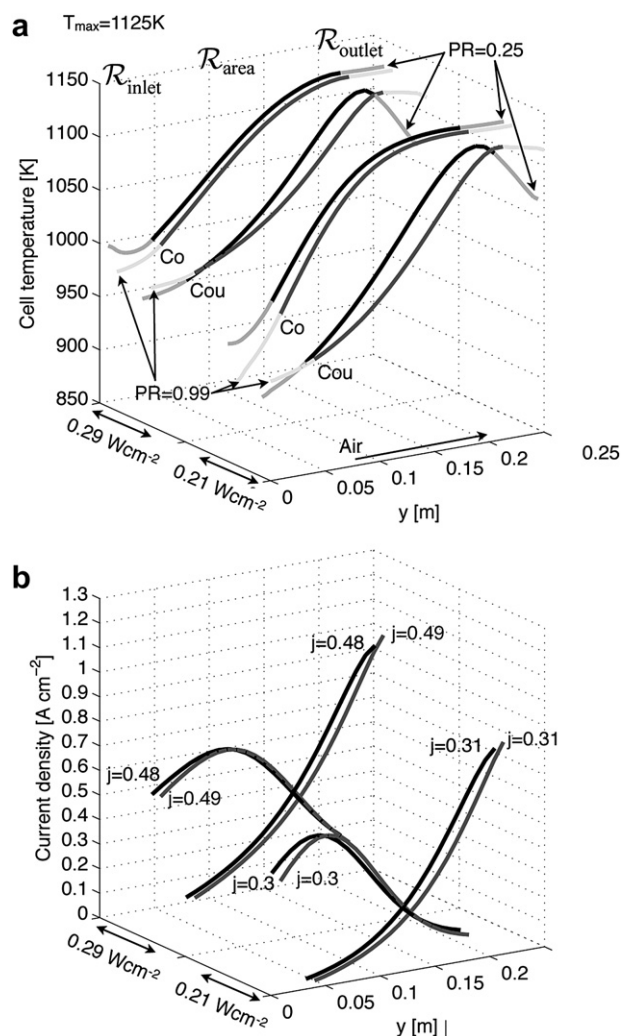


Fig. 5. (a) Temperature profiles over the SRU and (b) current density profiles over the active area corresponding to operating points selected from Fig. 4: maximum cell temperature of 1125 K, system specific power of 0.21 W cm<sup>-2</sup> and 0.29 W cm<sup>-2</sup> and methane conversion fraction in the reformer of 0.25 and 0.99. j in (b) refers to the average current density.

#### 4.1.2. Continuous decision variables

The needed air ratio scales with the system power but exhibits a maximum that occurs at a lower specific system power for lower maximum SRU temperatures (see Fig. 4a). At low specific system power, consequently air flow, the air inlet temperature is decreased because the in-plane thermal conductivity of the SRU is kept constant. Indeed, Fig. 5a shows that the temperature difference over the active area is similar at 0.21 W cm<sup>-2</sup> and 0.29 W cm<sup>-2</sup> in the co-flow configuration. In the counter-flow case, only part of the active area is effectively used at 0.21 W cm<sup>-2</sup>. The temperature at the air inlet of the active area can be therefore further decreased, as the electrochemical performance in this zone is less critical. In both flow configurations, the lower air blower consumption ensuing the reduction of the air ratio increases the system efficiency. At higher system specific power, the increase of the air inlet temperature is required for a more extensive use of the active area, but is balanced by the air blower parasitic consumption.

For fixed gas inlet temperatures and maximum SRU temperature, the temperature difference over the SRU scales with the specific system power, because of air flow increases. The previous discussion shows that this is not the case for practical system operating



conditions. The temperature difference is the highest at low system specific power, because of the low corresponding air inlet temperature. In co-flow (counter-flow) configuration, a complete (low) methane conversion fraction in the reformer is beneficial in terms of system electrical efficiency, but yields the highest temperature difference, because of the lower air inlet temperature.

The dependence of the optimised fuel utilisation on the specific system power density is indirectly affected by the maximum temperature. Diffusion losses exhibit a low temperature dependence compared with other contributions to the losses in an SOFC and scale with the current density. Higher maximum SRU temperature yields a better electrochemical performance of the MEA, hence higher voltage and lower current density and air flow for a given system power. The fuel utilisation, consequently system efficiency, increases as shown in Fig. 4c.

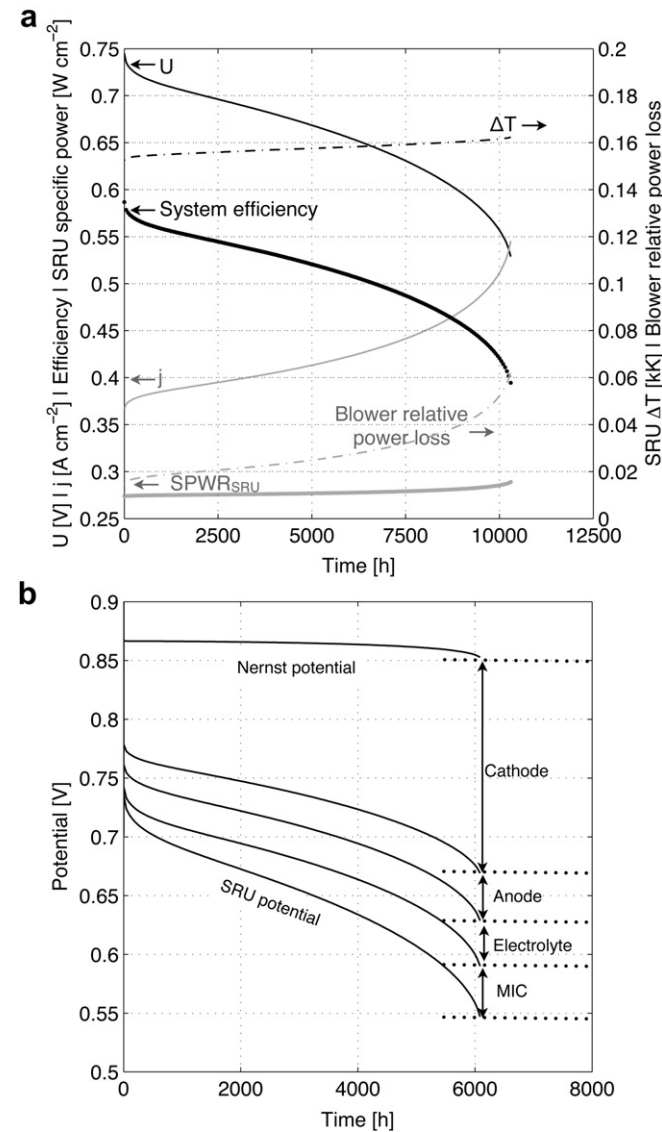


**Fig. 6.** (a) Typical evolution during operation at constant system power, of the system efficiency (left, Eq. (5)), SRU potential (left), current density (left), SRU specific power (left), temperature difference over the SRU (right) and relative blower power consumption, as a fraction of stack power (right). Counter-flow, maximum SRU temperature of 1125 K, methane conversion percentage in the reformer of 25% and system specific power of  $0.25 \text{ W cm}^{-2}$ . (b) Contributions to the total overpotential in the counter-flow configuration, at a constant specific system power of  $0.29 \text{ W cm}^{-2}$ , a maximum SRU temperature of 1125 K and methane conversion in the reformer of 25%. The Nernst potential is computed at the anode/electrolyte interface.

This analysis shows that comparing flow configurations in the light of identical inlet conditions is practically of limited interest. Structural aspects may limit the complete use of the benefits provided by operation at lower specific power, higher temperature and adjustments of the methane conversion fraction in the reformer.

#### 4.2. Long-term system electrical efficiency

The less stringent operation mode for an SOFC system is constant electrical power output at the highest efficiency. Even though this best-case scenario excludes any cycling, it is more demanding than most stack endurance tests, which are commonly performed at constant current density. This, along with the rather low performance of the LSM–YSZ cathode used for the calibration of the model [25] accounts for the short lifetimes predicted here.

During operation at constant system power and maximum allowable temperature, the SRU potential decreases because of the

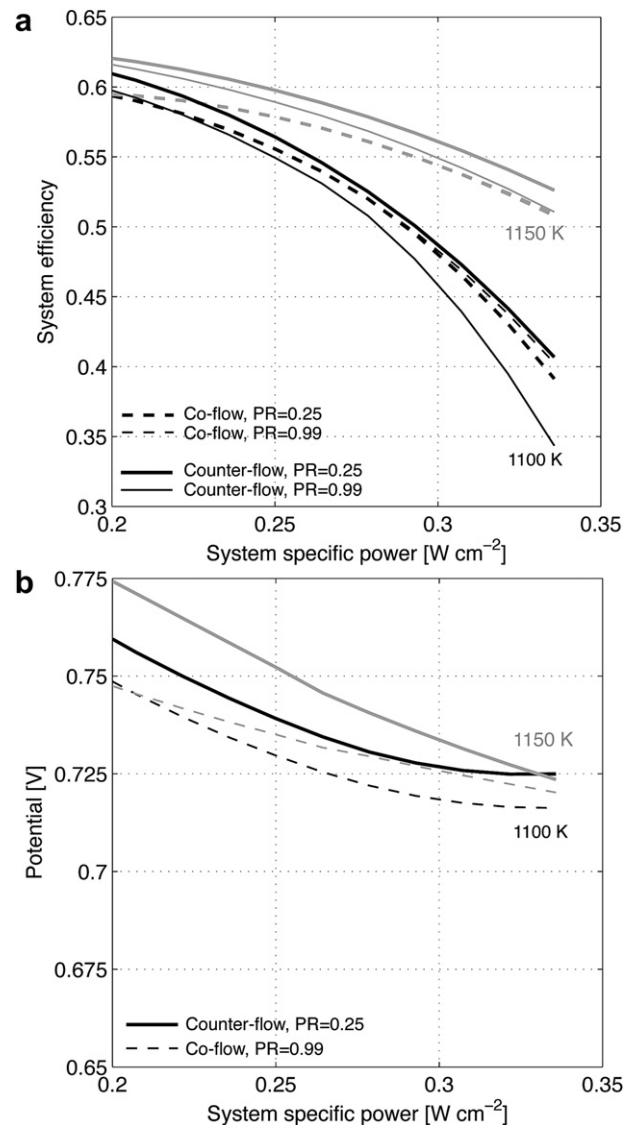


**Fig. 7.** (a) Initial system efficiency (Eq. (5)) and (b) cell potential vs. system specific power, resulting from the optimisation of the system efficiency at long-term under operation at constant system power. Co-flow (dashed lines) or counter-flow (continuous lines) configurations, with discrete maximum allowable cell temperatures of 1100 K (black) and 1150 K (grey), and methane conversion fraction in the reformer of 0.25 (thick lines) and 0.99 (thin lines).



degradation processes (see Fig. 6a). The current density must be ever increased, which causes higher internal polarisation losses. The air ratio increases to maintain the maximum SRU solids temperature limit. The temperature difference increases and tends towards the value determined by the air inlet temperature and maximum allowable temperature, except in co-flow configuration for low methane conversion. The higher air blower parasitic consumption must be in turn compensated by an increase of the current density. The acceleration of the regime after prolonged use induces the end of life of the device, which is further amplified by the sequential activation of multiple degradation processes (see Section 4.2.3). As discussed in detail in Ref. [20], the degradation pattern depicted in Fig. 6 has been observed in endurance tests of short stacks with anode-supported cells based on an LSM–YSZ cathode [18]. Experimental measurements do however not always exhibit the initial decay because of overlapping activation processes, which are not implemented in the model.

Fig. 6b depicts the contributions to the total overpotential and their evolution upon operation, of the cathode, anode, electrolyte and MIC. The contribution of the cathode dominates, which is the case for all the investigated cases (not depicted). Among the other contributions, that of the MIC exhibits the highest relative increase. Those of the anode and electrolyte are comparable (see Part II [26]).

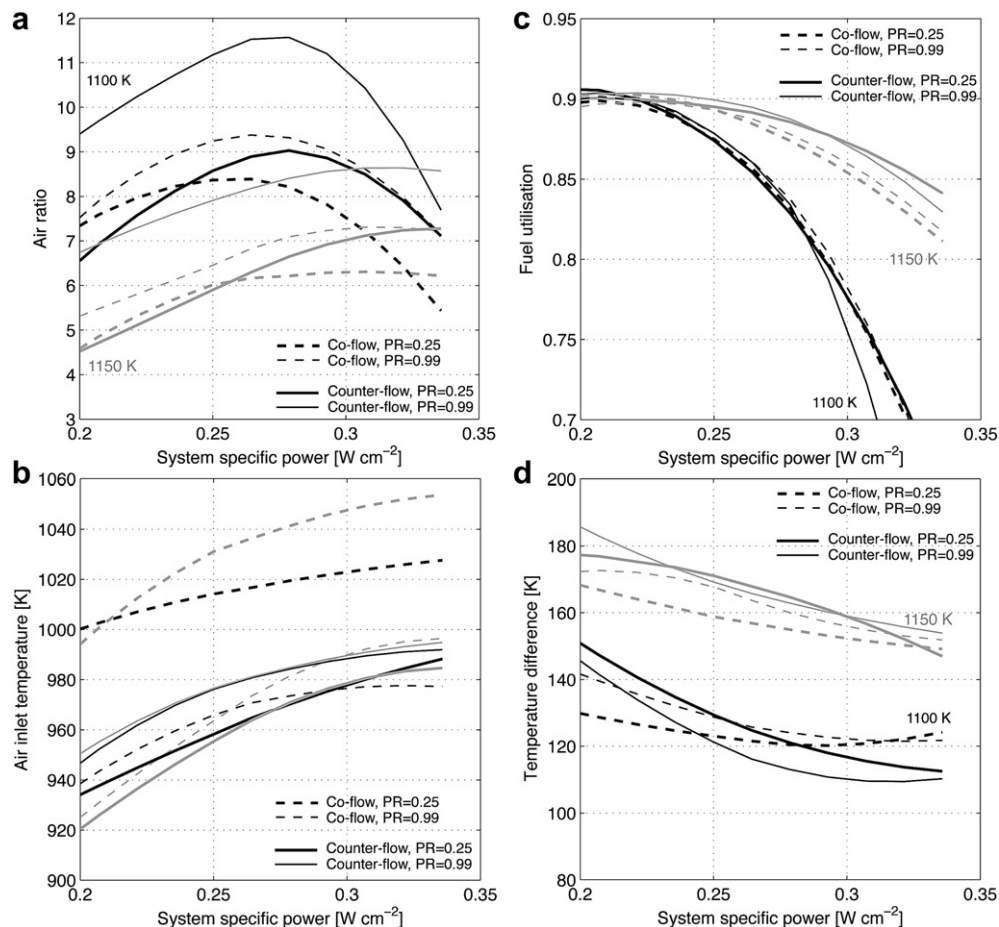
#### 4.2.1. Lifetime improvement

Fig. 7 depicts the initial performance that results from optimisation in the view of the highest system efficiency at long-term. In

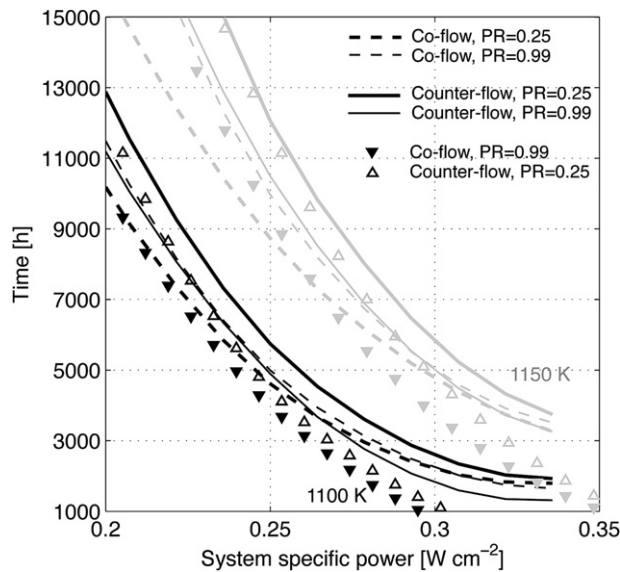
a first approximation, the optimiser favours the SRU potential over the initial system efficiency (compare Figs. 3 and 7). The effect of the maximum allowable temperature and methane conversion fraction in the reformer is similar to that described in Section 4.1. In co-flow configuration, a complete conversion is slightly beneficial.

Fig. 8 depicts the optimum values of the continuous decision variables. The optimiser reduces the fuel utilisation to extend the lifetime. The main reason is not the degradation of the anode, as in the model the nickel particle radius reaches its plateau value on most of the active area before 2000 h (see Part II [26]), but the mitigation of the progressive increase of the current density and air ratio during operation, while allowing a slight increase of the air inlet temperature to lower the cathode overpotential. This results in a larger difference between the system electrical efficiency at start and at long term for a lower maximum SRU temperature and a dependence of this difference on the second objective, the system specific power (see Fig. 7). It also accounts for the decrease of the temperature difference over the SRU (compare Figs. 4d and 8d).

Fig. 9 and Table 3 provide the effect of the operating conditions and their optimisation on the lifetime, defined here as the time to reach a drop in system efficiency of 20%. The computed lifetime extension is provided here for presentation purpose. The model limitations discussed in Section 2 and incomplete understanding of the degradation phenomena affecting SOFCs limit their applicability to all cases. The counter-flow configuration along with the highest maximum SRU temperature (1150 K) and lowest methane conversion fraction in the reformer ( $PR = 0.25$ ) results in the



**Fig. 8.** Operating conditions to achieve the highest system efficiency at long-term as a function of the system specific power (Fig. 7): (a) air ratio, (b) stack air inlet temperature, (c) fuel utilisation, and (d) resulting temperature difference over the SRU, with fixed maximum allowable cell temperatures of 1100 K (black) and 1150 K (grey), and amount of fuel pre-reforming (line thickness). The largest discrepancy between the trend line and the actual result is 7% (air ratio).



**Fig. 9.** Effect of the operating conditions depicted in Fig. 4 (markers) and Fig. 8 (lines) on the degradation of the system efficiency. Operating time at constant system power leading to a decrease in efficiency of 20%, for the co-flow (dashed lines) or counter-flow (solid line) configuration, with a maximum allowable cell temperature of 1100 K (black) and 1150 K (grey). The largest discrepancy between the trend line and the actual result is 10%.

highest lifetime and averaged system efficiency over the investigated system specific power range. The gain in lifetime obtained by manipulating optimised operating conditions are listed hereafter, from the most to the less significant effect:

- System specific power: factor around 4 ( $0.21 \text{ W cm}^{-2}$  vs.  $0.28 \text{ W cm}^{-2}$ ).
- Maximum SRU temperature: factor around 2 (1150 K vs. 1100 K).
- Methane conversion fraction: factor around 1.3 (PR = 0.25 vs. PR = 0.99, depending on flow-configuration).
- Flow configuration: factor around 1.2 (counter vs. co-flow).

In the conditions treated here, the degradation of the cathode dominates. Lower cathode overpotentials, which is a driving force for Cr deposition and also zirconate formation can be obtained by adjusting the system specific power, maximum SRU and air inlet temperature and flow configuration. The benefit of decreasing the overpotential prevails over the higher vaporisation rate of volatile chromium species from the MIC, higher relative degradation of the conductivity of YSZ and higher thermodynamic risks of zirconate formation. Manipulation of the methane conversion fraction is a mean to lower the air ratio, consequently the increase of the system parasitic losses to maintain the specified maximum solid

temperature as the degradation proceeds. The counter-flow configuration limits interactions between the degradation phenomena at the SRU scale compared with the co-flow configuration (see Section 4.2.3 for anode reoxidation and Part II for anode and electrolyte degradation promoted by the evolution of the current density and temperature distribution). The aspects are discussed in more details in the next Sections.

Our structural analyses [27,28] have furthermore shown that all these manipulations can be opposite to those that promote mechanical reliability and durability, resulting in trade-offs between electrochemical and mechanical considerations.

#### 4.2.2. Effects of manipulations of the operating conditions on the lifetime

Fig. 10 depicts the effect of methane conversion in the reformer, maximum SRU temperature, assigned system power and flow configuration on the evolution of the system efficiency. The pattern of the degradation is independent of the operating conditions. The degradation curves of the system efficiency under the operating conditions optimised for the best initial performance are depicted for a specific system power of  $0.29 \text{ W cm}^{-2}$  (group of light grey curves A, Fig. 10). The effects of the maximum SRU temperature, the methane conversion fraction in the reformer and the flow configuration, are consistent with Fig. 9 (see Section 4.2.1).

**4.2.2.1. System specific power.** Decreasing the specific power is expected to have a beneficial effect on the cost of electricity, because it promotes higher electrical efficiency and the gain in lifetime achieved by lowering the cathode overpotential largely compensates the lower power, in terms of produced electrical energy.

Mechanical reliability, application-related, manufacturing and/or costs considerations that are not included in the present optimisation problem may limit the advantages of these adjustments. For example, operation at a low specific power to extend the lifetime requires to stack more elements to achieve the targeted system power. This increases (i) the costs, (ii) the risks of cell cracking, due to the larger volume of brittle ceramic material subjected to thermal stress, and (iii) gas distribution issues among the stacked SRU. The lack of reproducibility of the mechanical properties of the component materials and dimensional tolerances amplifies all these aspects. In this view, Table 4 and the comparison between lines and markers in Fig. 9 suggests the significant benefit of targeting higher long-term efficiency on the lifetime, by a factor up to 3.5, by optimising the air inlet temperature and fuel utilisation for given system specific power, maximum SRU temperature, methane conversion fraction in the reformer and flow configuration.

**4.2.2.2. Operating temperature.** A higher operating temperature promotes extended lifetime by reducing the cathode overpotential, which is a driving force for both the electrochemical deposition of  $\text{Cr}_2\text{O}_3$  at the TPB and formation of LZO/SZO (20), and to a lesser

**Table 3**  
Lifetime extension factors obtained by manipulating operating conditions, from Fig. 8 (highest long-term system efficiency). The lifetime is determined as the time to reach a decrease in system efficiency of 20%. Inside parentheses is the averaged system efficiency over the lifetime and produced electrical energy ( $\text{kW h cm}^{-2}$ ).

	1100 K	1125 K	1150 K
Co-flow, $0.29 \text{ W cm}^{-2}$ , PR = 0.25	1.00 <sup>a</sup> (0.441, 0.71)	1.53 (0.475, 1.09)	2.14 (0.493, 1.52)
Co-flow, $0.29 \text{ W cm}^{-2}$ , PR = 0.99	1.06 (0.440, 0.75)	1.73 (0.474, 1.23)	2.43 (0.493, 1.73)
Co-flow, $0.21 \text{ W cm}^{-2}$ , PR = 0.99	4.04 (0.535, 2.08)	5.92 (0.542, 3.05)	8.02 (0.539, 4.13)
Counter-flow, $0.29 \text{ W cm}^{-2}$ , PR = 0.25	1.18 (0.446, 0.84)	2.00 (0.480, 1.42)	2.63 (0.506, 1.87)
Counter-flow, $0.29 \text{ W cm}^{-2}$ , PR = 0.99	0.92 (0.421, 0.65)	1.69 (0.466, 1.20)	2.18 (0.495, 1.55)
Counter-flow, $0.21 \text{ W cm}^{-2}$ , PR = 0.25	4.67 (0.545, 2.40)	7.14 (0.553, 3.68)	9.71 (0.562, 5.00)

<sup>a</sup> Reference case for the calculation of the lifetime extension factor.

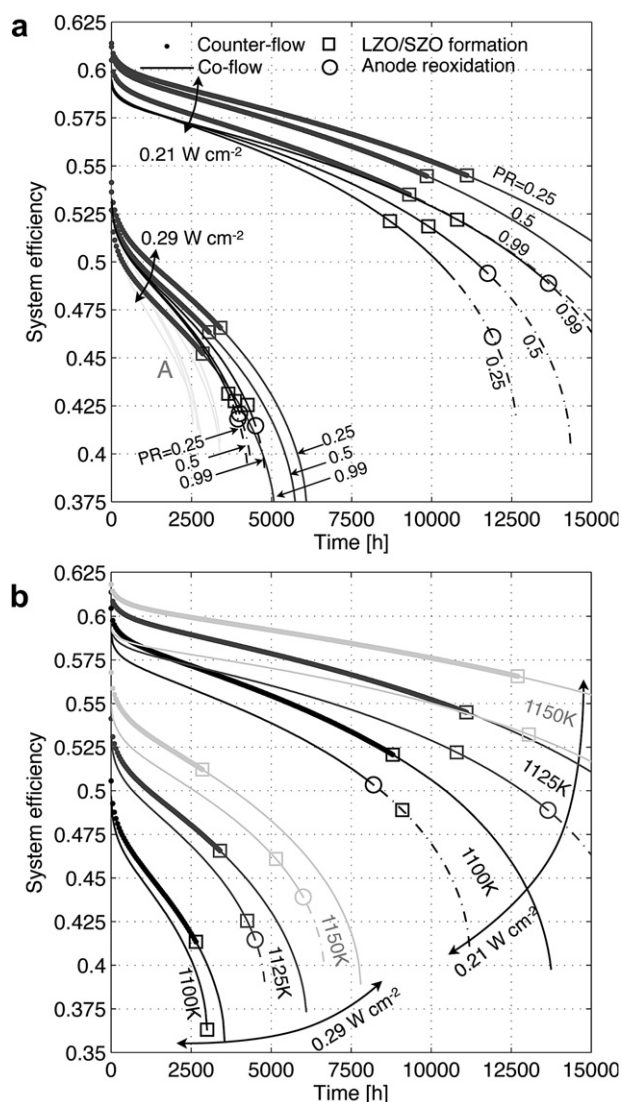


**Fig. 10.** Effect of (a) the amount of pre-reformed methane and (b) maximum allowable cell temperature (co-flow: PR = 0.99, counter-flow: PR = 0.25) on the degradation of the system efficiency, for the co-flow or counter-flow configuration, with the operating conditions depicted in Fig. 8, except the light grey curves (top, A, see text) (Fig. 4). The occurrence, from thermodynamic consideration, of anode reoxidation and possible formation of LZO/SZO is indicated by empty markers. Constant specific system power of  $0.21 \text{ W cm}^{-2}$  and  $0.29 \text{ W cm}^{-2}$ .

extent by reducing the parasitic air blower consumption. This trend is balanced by an accelerated increase of the MIC ASR, due to a faster growth of the oxide scale, even in the presence of a protective coating (see Section 2), higher internal vaporisation of

volatile chromium species from the MIC, higher relative degradation of 8YSZ, and thermodynamic risk of zirconate formation. In the conditions treated here, the benefits of operation at higher temperature prevail over the drawbacks. Investigations with the present modelling approach, but different operating conditions, suggest that the maximum lifetime value is around 1180 K [59], which qualitatively matches the operating temperature of stacks with electrolyte-supported cells and coated MICs, e.g. Ref. [60]. The air inlet temperature has similarly opposite effects on the degradation of an LSM–YSZ cathode. Its increase yields a higher inlet  $p_{\text{CrO}_2(\text{OH})_2}$  and higher air blower parasitic consumption but helps to avoid high local cathode overpotentials.

**4.2.2.3. Methane conversion fraction in the reformer.** The influence of methane conversion fraction in the reformer is opposite in the co-flow and counter-flow configurations (Section 4.2.1). High conversion values are detrimental (beneficial) in the counter-flow (co-flow) configuration. Despite the discrete nature of this decision variable in the optimisation problem, the dependence is likely monotonic over the considered range of variation, as suggested by Fig. 10.

#### 4.2.3. Progressive activation of degradation processes

The impact of the reoxidation of the anode and formation of LZO/SZO in the LSM–YSZ cathode on the electrochemical performance is neither modelled nor included as end-constraints in the optimisation problem. The markers in Fig. 10 indicate the time at which these phenomena are thermodynamically activated and would accelerate the degradation. The reoxidation of the anode does not occur in counter-flow configuration under the conditions studied here, owing to the location of the maximum local current density close to the fuel inlet zone of the active area, where the hydrogen concentration and temperature are the highest. In co-flow, it is activated after the formation of zirconates and can be practically avoided by adjusting the fuel utilisation. It arises from the progressive increase of the current density and occurs first at the anode/electrolyte interface in the zones where the fuel is depleted. The lifetime defined as the time at which anode reoxidation may take place, qualitatively follows the same trend as in Fig. 9 (not depicted).

Fig. 11 depicts the dependence of the operating time at which zirconate can form in the operating conditions. The effect of the operating temperature is governed by a trade-off between (i) lower cathode overpotential and (ii) the thermodynamic promotion of the formation of zirconate in the LSM–YSZ system at high temperature, and oxygen partial pressure at the cathode/electrolyte interface (see Part II [26]). The effect of (i) dominates that of (ii) over the investigated range. For a given maximum SRU temperature and system specific power, the co-flow configuration provides better overall resistance, since the zone of high cathode overpotential is subjected to lower temperature. Even though the formation of LZO/SZO is not included in the optimisation problem, it is delayed by the reduction of the overpotential to alleviate the chromium contamination of the cathode.

The aforementioned results highlight the importance of the cathode overpotential on the degradation of the performance. Fig. 12 shows the maximum local cathode overpotentials induced by the operating conditions optimised for the highest system efficiency at start (Figs. 3 and 4) and long-term (Figs. 7 and 8). The trade-off between temperature and anode gas composition in the co-flow case induces significantly higher cathode overpotential than in the counter-flow case. The optimisation of the long-term system efficiency clearly favours lower cathode overpotential, by a slight increase of the air inlet temperature and reduction of the fuel utilisation that alleviates the constraint of the distribution of

**Table 4**

Lifetime extension factors from the optimisation of the operating conditions, i.e. ratio between the conditions depicted in Fig. 8 (highest long-term system efficiency) and Fig. 4 (highest system efficiency at start), for given system specific powers and maximum SRU temperatures. The lifetime is defined as the time to reach a decrease in system efficiency of 20%.

	1100 K	1125 K	1150 K
Co-flow, $0.29 \text{ W cm}^{-2}$ , PR = 0.25	2.88	1.44	1.67
Co-flow, $0.29 \text{ W cm}^{-2}$ , PR = 0.99	2.26	1.73	1.43
Co-flow, $0.21 \text{ W cm}^{-2}$ , PR = 0.99	1.05	1.20	1.08
Counter-flow, $0.29 \text{ W cm}^{-2}$ , PR = 0.25	1.81	1.63	1.28
Counter-flow, $0.29 \text{ W cm}^{-2}$ , PR = 0.99	3.46	1.63	1.15
Counter-flow, $0.21 \text{ W cm}^{-2}$ , PR = 0.25	1.11	1.06	1.05



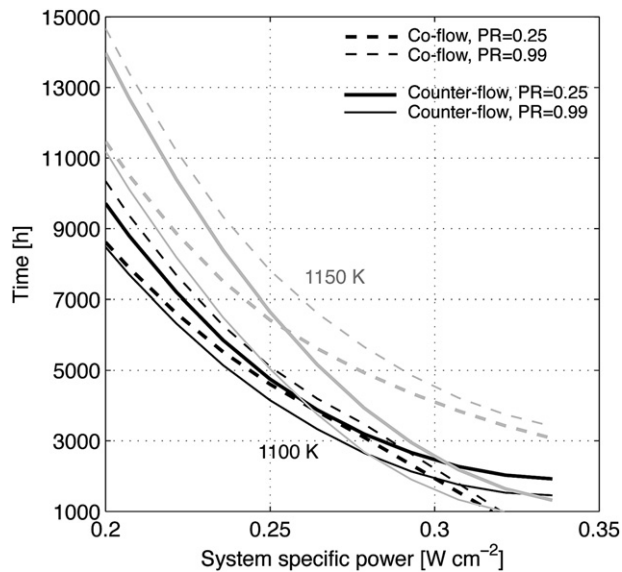


**Fig. 11.** Operating time at constant system power, before the possible formation of zirconates in the LSM–YSZ cathode, in an SRU operated in co-flow (dashed lines) or counter-flow (solid lines) configuration. Conditions from Fig. 8. The maximum allowable cell temperature of 1100 K and 1150 K is indicated by grey scale variation and the methane conversion fraction in the reformer by line thickness. The largest discrepancy between the trend line and the actual result is 13%.

the gas composition over the active area on that of the current density. The effects of the maximum SRU temperature and methane conversion fraction in the reformer are minor at the initial time, but are amplified by ageing. The dependence of the maximum cathode overpotential on the decision variables and system specific power follow similar trends than the lifetime.

#### 4.3. Effect of system operation and cathode performance

Endurance tests of SOFC stacks are commonly performed at constant current density [18,61], which is favourable for the stack lifetime but does not fully reflect field conditions. Fig. 13 shows the difference between operation at constant potential, current density and system specific power. Testing conditions strongly influence the observed degradation and evolution of the air ratio. The reoxidation of the anode and formation of LZO/SZO do not occur during operation at constant potential, owing to the small variation of the cathode overpotential and monotonic decrease of the current density. For the same reasons, the air ratio, hence temperature difference, decreases. The reoxidation of the anode may occur at constant current density, in the co-flow configuration, due to the redistribution of the current density. As the cathode performance decreases, the zone of highest current density is shifted towards zones of higher temperature and lower hydrogen molar fraction. This is not the case in the counter-flow configuration.

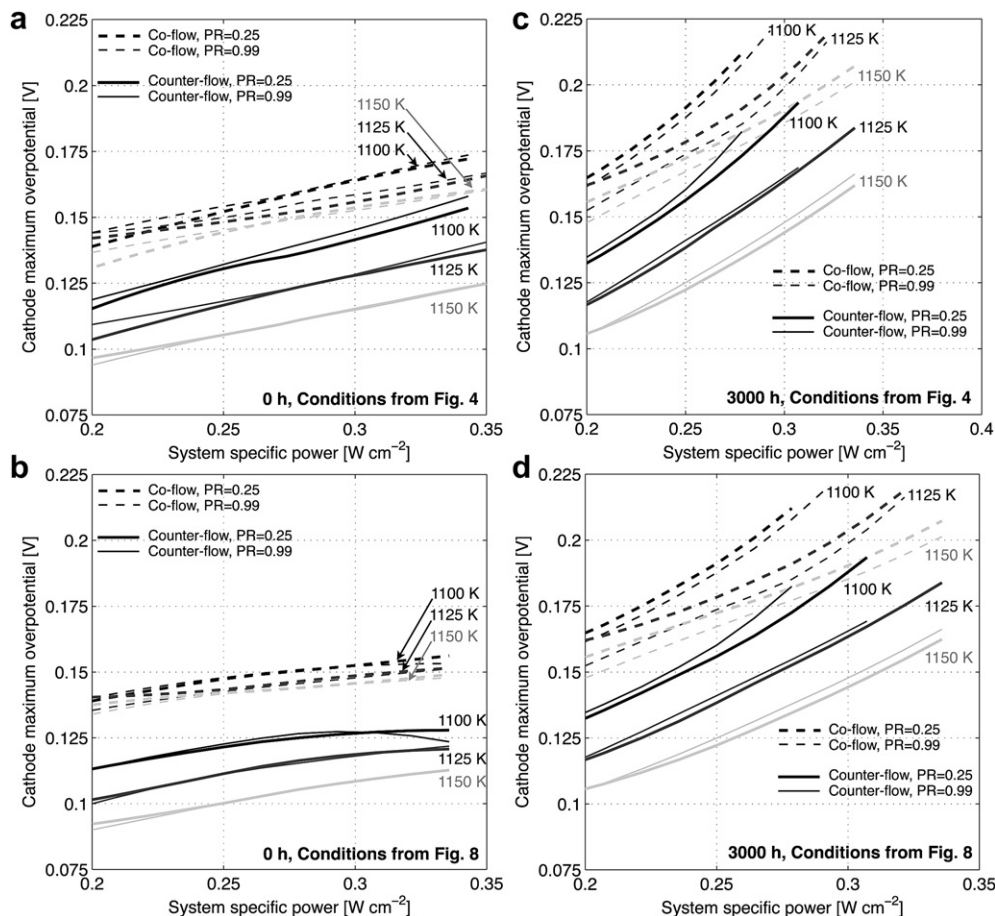


**Fig. 12.** Maximum local cathode overpotential at the initial time (a, b) and after 3000 h of operation at a constant system power (c, d), under the conditions depicted in Figs. 4 and 8, for the co-flow (dashed lines) or counter-flow (solid lines) configuration, with different discrete maximum allowable cell temperatures (grayscale variations) and methane conversion fraction in the reformer (line thickness). The largest discrepancy between the trend line and the actual result is 6.5%.



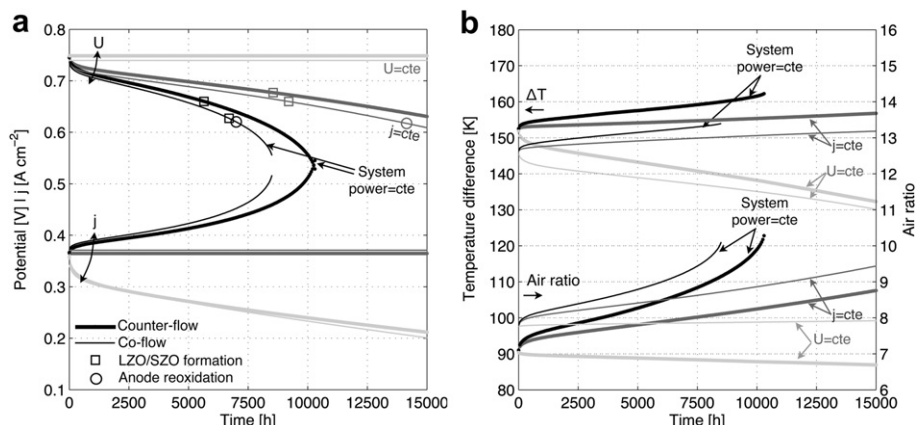


**Fig. 13.** Comparison of (a) the evolution of the SRU potential, current density, specific power, (b) temperature difference and air ratio, during operation at constant potential (light grey), current density (grey) and system power (black), for the co-flow (PR = 0.99) and counter-flow (PR = 0.25) configurations. The maximum cell temperature is 1125 K. An identical initial cell potential is enforced among the operating scenario, yielding an initial system specific power of  $0.25 \text{ W cm}^{-2}$ . Empty markers indicate the occurrence of anode reoxidation and possible formation of LZO/SZO.

The combined influence of the air ratio, air inlet temperature and fuel utilisation identified in Section 4.1.1 underscores the importance of including system considerations in lifetime analyses. The parasitic consumption of the air blower is related to the stack pressure drop. Fig. 14 shows that the system pressure drop has a significant effect on the degradation of the system efficiency. For this comparison, the stack specific power, rather than the system specific power is kept constant to enforce identical initial SRU conditions, i.e. overpotentials. A stack and interconnection design for extended lifetime must therefore consider pressure drop in the light of (i) the supply of reactant to the active sites and current constriction effects in the interconnection system, (ii) the need of a homogeneous in-plane gas distribution, (iii) the benefits of lower system parasitic consumptions and (iv) the mechanical stability of the GDL and sealants.

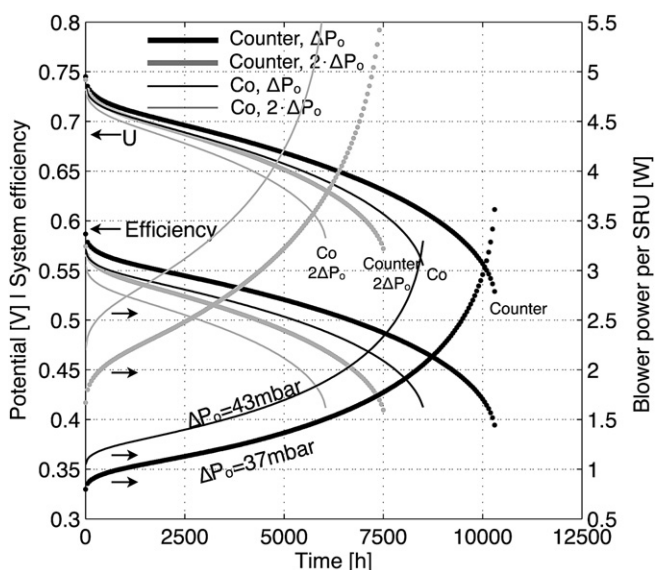


**Fig. 14.** Effect of the system pressure drop on the evolution of the system efficiency, SRU potential and blower consumption per SRU, during operation at a constant system specific power of approximately  $0.25 \text{ W cm}^{-2}$ , the identical initial SRU power is enforced among the nominal and high pressure drop cases. Co-flow: PR = 0.99, counter-flow: PR = 0.25.

## 5. Conclusion

The developed modelling approach aims at supporting stack and system design and operation for extended durability. This study has placed the emphasis on the effect of the operation conditions on the degradation of SOFC stacks integrated in a system, under practical constant system electrical power output mode. Optimisation has shed light on critical decision variables, their inter-dependences and the differences between the requirements for the highest system electrical efficiency at start-up and at long-term.

The degradation processes detrimentally interact in an SRU. Under practical operating conditions, their sequential activation shortens the lifetime of the device. The loss of performance due to chromium contamination of an LSM–YSZ cathode can activate the formation of LZO/SZO insulating phases. Reoxidation of the anode can occur in the co-flow configuration if the fuel utilisation is not adjusted upon operation, because of the increase of the current density to deliver a constant system electrical power output. It did not occur during the simulations in counter-flow configuration. The system, through the air blower parasitic consumption, also plays an important role in the system efficiency degradation.

Besides material improvements, the manipulation of the operating parameters is an effective and practical means to improve the durability, which, like system electrical efficiency, scales inversely with the system specific power. The gain in lifetime largely compensates for the decrease in specific power, in terms of produced electricity. The lower maximum cathode overpotential in counter-flow and the effect of internal reforming on lowering the parasitic air blower consumption is beneficial since it alleviates in the long-term cathode chromium contamination, risk of anode reoxidation and zirconate formation in the cathode. In reality, mechanical, application, manufacturing and/or costs considerations may limit the advantages of these adjustments. Examples that are not considered in the model are gas flow distribution problems arising from the need to increase the number of SRU in the stack and larger irreversible deformation generated at high temperature. Future stress analysis is needed to better characterise the trade-off between electrochemical and mechanical degradation. In this view, the separate optimisation of the air inlet temperature and fuel utilisation in the view of long-term, instead of initial system electrical efficiency, further extends the durability (factor up to 3.5).

The present study only partially addresses the complexity of SOFC degradation, because the underlying physics is highly dependent on the materials and application, and deeper understanding is in progress. It however reveals the potential for considerable durability improvements. To extend the knowledge and push further the current limitations of the SOFC technology,

- Relevant analyses must include the interactions between the various phenomena that affect SOFC degradation.
- Control and operation strategies, as well as system integration, must be integrated with lifetime analysis.
- Modelling and experimental tasks must be carried out in synergy.

## Acknowledgements

This work was funded by the Swiss SOFC Consortium, co-financed by the Swiss Federal Office of Energy (SFOE) and Swiss-electric Research, contract number 152210, and the FP6 FLAME-SOFC European project, contract number CE-Flame SOFC-019875. gPROMS, a modelling tool from Process System Enterprise (PSE) has been used under academic licensing. Computations have been performed on the Pleiades2 cluster located at EPFL.

## Nomenclature

### Latin letters

$\dot{N}$	molar flow rate ( $\text{mol s}^{-1}$ )
$\mathcal{P}$	specific power ( $\text{W m}^{-2}$ )
$\mathcal{V}$	volume ( $\text{m}^3$ )
$\mathcal{R}_i$	rate of production of species $i$ ( $\text{mol m}^{-3} \text{s}^{-1}$ )
LHV	lower heating value ( $\text{J mol}^{-1}$ )
$A$	area ( $\text{m}^2$ )
$A_{\text{TPB}}$	specific area at the triple phase boundary ( $\text{m}^2 \text{m}^{-3}$ )
$B_o$	permeability in porous medium ( $\text{m}^2$ )
$D_{ij}^e$	effective bulk diffusivity of binary pair in porous medium ( $\text{m}^2 \text{s}^{-1}$ )
$E_a$	activation energy ( $\text{J mol}^{-1}$ )
$F$	Faraday's constant 96,485 ( $\text{C mol}^{-1}$ )
$h$	thickness (m)
$i_o$	exchange current density ( $\text{A m}^{-2}$ )
$k_o$	kinetic constant
$K_{\text{eq}}$	equilibrium constant, dimensionless
$L$	length (m)
$m^{\text{crp}}$	creep stress exponent
$n$	porosity
$n_t$	exponent
$Nu$	Nusselt number
$P$	power (W)
$p$	pressure (Pa)
$p^{\text{atm}}$	atmospheric pressure 101,325 (Pa)
$R$	universal gas constant 8.314 ( $\text{J mol}^{-1} \text{K}^{-1}$ )
$T_{\text{amb}}$	ambient temperature, 298 (K)
$u$	gas velocity ( $\text{m s}^{-1}$ )
$x_i$	mole fraction of species $i$

### Greek letters

$\epsilon$	strain
$\epsilon^{\text{eff}}$	efficiency
$\eta$	overpotential (V)
$\gamma$	ratio of specific heats ( $c_p/c_v$ )
$\mu_g$	viscosity (Pa s)
$\rho$	density ( $\text{kg m}^{-3}$ )
$\sigma$	stress (Pa)

### Indices

$\mathcal{D}$	degradation
blwr	blower
cath	cathode
eq	equivalent
o	initial, dense state
out	outlet
s	index for solid parts, individual components or averaged structure
sys	system

### Superscripts

*	foam
crp	creep
dep	deposition
vap	vaporation

### Acronyms

ASR	area specific resistance
CHP	combined heat and power generation
COU	counter-flow
CO	co-flow
EIS	electrochemical impedance spectra
GDL	gas diffusion layer
LSCF	lanthanum strontium cobaltite ferrite
LSM	lanthanum strontium manganite
LZO	lanthanum zirconate
MEA	membrane electrode assembly
MIC	metallic interconnect
SRU	single repeating unit
SZO	strontium zirconate
TPB	triple phase boundary
YSZ	yttria-stabilised zirconia

## References

- [1] K. Nanaeda, F. Mueller, J. Brouwer, S. Samuelsen, Journal of Power Sources 195 (2010) 3176–3185.
- [2] S. Koch, P. Hendriksen, M. Mogensen, Y. Liu, N. Dekker, B. Rietveld, B. de Haart, F. Tietz, Fuel Cells 6 (2006) 130–136.
- [3] A. Hagen, R. Barfod, P. Hendriksen, Y. Liu, S. Ramousse, Journal of the Electrochemical Society 153 (2006) A1165–A1171.
- [4] F. Mueller, F. Jabbari, J. Brouwer, Journal of Power Sources 187 (2009) 452–460.
- [5] F. Mueller, R. Gaynor, A.E. Auld, J. Brouwer, F. Jabbari, G.S. Samuelsen, Journal of Power Sources 176 (2008) 229–239.
- [6] D. Simwonis, F. Tietz, D. Stöver, Solid State Ionics 132 (2000) 241–251.
- [7] R. Vaßen, D. Simwonis, D. Stöver, Journal of Materials Science 36 (2001) 147–151.
- [8] P. Tanasini, M. Cannarozzo, P. Costamagna, A. Faes, J. Van herle, A. Hessler-Wyser, C. Comninellis, Fuel Cells 9 (2009) 740–752.
- [9] A. Faes, A. Hessler-Wyser, D. Presvytes, C. Vayenas, J. Van herle, Fuel Cells 9 (6) (2009) 841–851.
- [10] L. Holzer, B. Iwanschitz, T. Hocker, B. Münch, M. Prestat, D. Wiedenmann, U. Vogt, P. Holtappels, J. Sfeir, A. Mai, T. Graule, Journal of Power Sources 196 (2011) 1279–1294.
- [11] L. Holzer, B. Iwanschitz, M. Cantoni, T. Hocker, T. Graule, 2010, Journal of Power Sources 196 (17) (2011) 7076–7089.
- [12] Y. Liu, A. Hagen, R. Barfod, M. Chen, H. Wang, F. Poulsen, P. Hendriksen, Solid State Ionics 180 (2009) 1298–1304.
- [13] P. Batfalsky, V. Haanappel, J. Malzbender, N. Menzler, V. Shemet, I. Vinke, R. Steinbrech, Journal of Power Sources 155 (2006) 128–137.
- [14] F. Wiener, M. Bram, H. Buchkremer, D. Sebold, Journal of Materials Science 42 (2007) 2643–2651.
- [15] Y.L. Liu, S. Primdahl, M. Mogensen, Solid State Ionics 161 (2003) 1–10.
- [16] H. Yokokawa, H. Tu, B. Iwanschitz, A. Mai, Journal of Power Sources 182 (2008) 400–412.
- [17] K. Ogasawara, H. Kameda, Y. Matsuzaki, T. Sakurai, T. Uehara, A. Toji, N. Sakai, K. Yamaji, T. Horita, H. Yokokawa, Journal of the Electrochemical Society 154 (2007) B657–B663.
- [18] L. de Haart, J. Mougou, O. Posdziech, J. Kiviahio, N. Menzler, Fuel Cells 9 (2009) 794–804.

- [19] M. Fardadi, F. Mueller, F. Jabbari, *Journal of Power Sources* 195 (2010) 4222–4233.
- [20] A. Nakajo, P. Tanasini, S. Diethelm, J. Van herle, D. Favrat, *Journal of the Electrochemical Society* 158 (2011) B1102–B1118.
- [21] D. Larrain, J. Van herle, D. Favrat, *Journal of Power Sources* 161 (2006) 392–403.
- [22] Z. Wuillemin, 2009, Experimental and Modeling Investigations on Local Performance and Local Degradation in Solid Oxide Fuel Cells, Ph.D. thesis, Lausanne, 4525 pp.
- [23] Z. Wuillemin, N. Autissier, A. Nakajo, M.-T. Luong, J. Van herle, D. Favrat, *Journal of Fuel Cell Science and Technology* 5 (2008) 011016–011019.
- [24] J. Gazzarri, O. Kesler, *Journal of Power Sources* 176 (2008) 138–154.
- [25] A. Nakajo, Z. Wuillemin, P. Metzger, S. Diethelm, G. Schiller, J. Van herle, D. Favrat, *Journal of the Electrochemical Society* 158 (2011) B1083–B1101.
- [26] A. Nakajo, F. Mueller, J. Brouwer, J. Van herle, D. Favrat, Progressive activation of degradation processes in solid oxide fuel cell stacks: Part II: Spatial distribution of the degradation, 2012, in this issue.
- [27] A. Nakajo, F. Mueller, J. Brouwer, J. Van herle, D. Favrat, *International Journal of Hydrogen Energy* 37 (2012) 9249–9268.
- [28] A. Nakajo, F. Mueller, J. Brouwer, J. Van herle, D. Favrat, *International Journal of Hydrogen Energy* 37 (2012) 9269–9286.
- [29] gPROMS (General Process Modelling and Simulation Tool), v3.2, Process Systems Enterprise Ltd., London.
- [30] F.H. van Heuveln, H.J.M. Bouwmeester, *Journal of the Electrochemical Society* 144 (1997) 134–140.
- [31] S.B. Adler, J.A. Lane, B.C.H. Steele, *Journal of the Electrochemical Society* 143 (1996) 3554–3564.
- [32] A.M. Svensson, S. Sunde, K. Nişancioglu, *Journal of the Electrochemical Society* 145 (1998) 1390–1400.
- [33] E. Achenbach, E. Riensche, *Journal of Power Sources* 52 (1994) 283–288.
- [34] H. Zhu, R.J. Kee, V.M. Janardhanan, O. Deutschmann, D.G. Goodwin, *Journal of the Electrochemical Society* 152 (2005) A2427–A2440.
- [35] W. Liu, X. Sun, E. Stephens, M. Khaleel, *Journal of Power Sources* 189 (2009) 1044–1050.
- [36] S.P. Jiang, J.P. Zhang, L. Apateanu, K. Foger, *Journal of the Electrochemical Society* 147 (2000) 4013–4022.
- [37] S.P. Jiang, J.P. Zhang, K. Foger, *Journal of the Electrochemical Society* 147 (2000) 3195–3205.
- [38] S.P. Jiang, J.P. Zhang, K. Foger, *Journal of the Electrochemical Society* 148 (2001) C447–C455.
- [39] J.W. Fergus, *International Journal of Hydrogen Energy* 32 (2007) 3664–3671.
- [40] A. Hagen, Y.L. Liu, R. Barfod, P.V. Hendriksen, *Journal of the Electrochemical Society* 155 (2008) B1047–B1052.
- [41] J. Nielsen, A. Hagen, Y. Liu, *Solid State Ionics* 181 (2010) 517–524.
- [42] E. Konyshova, H. Penkalla, E. Wessel, J. Mertens, U. Seeling, L. Singheiser, K. Hilpert, *Journal of the Electrochemical Society* 153 (2006) A765–A773.
- [43] T. Horita, Y. Xiong, M. Yoshinaga, H. Kishimoto, K. Yamaji, M.E. Brito, H. Yokokawa, *Electrochemical and Solid-State Letters* 12 (2009) B146–B149.
- [44] F. Mueller, F. Jabbari, R. Gaynor, J. Brouwer, *Journal of Power Sources* 172 (2007) 308–323.
- [45] N. Dukhan, *Experiments in Fluids* 41 (2006) 665–672.
- [46] F. Incropera, D. DeWitt, T. Bergman, A. Lavine, 1996.
- [47] E. Opila, N. Jacobson, D. Myers, E. Copland, *JOM Journal of the Minerals, Metals and Materials Society* 58 (2006) 22–28.
- [48] B.B. Ebbinghaus, *Combustion and Flame* 93 (1993) 119–137.
- [49] B.B. Ebbinghaus, *Combustion and Flame* 101 (1995) 311–338.
- [50] J. Froitzheim, G. Meier, L. Niewolak, P. Ennis, H. Hattendorf, L. Singheiser, W. Quadackers, *Journal of Power Sources* 178 (2008) 163–173.
- [51] G.R. Holcomb, D.E. Alman, *Scripta Materialia* 54 (2006) 1821–1825.
- [52] N.H. Menzler, L.G. de Haart, D. Sebold, *ECS Transactions* 7 (2007) 245–254.
- [53] A. Neumann, N.H. Menzler, I. Vinke, H. Lippert, *ECS Transactions* 25 (2009) 2889–2898.
- [54] D. Larrain, J. Van herle, F. Maréchal, D. Favrat, *Journal of Power Sources* 131 (2004) 304–312.
- [55] B. Kuhn, C.A. Jimenez, L. Niewolak, T. Huttel, T. Beck, H. Hattendorf, L. Singheiser, W. Quadackers, *Materials Science and Engineering A* 528 (2011) 5888–5899.
- [56] N. Autissier, F. Palazzi, F. Marechal, J. Van herle, D. Favrat, *Journal of Fuel Cell Science and Technology* 4 (2007) 123–129.
- [57] D. Larrain, 2005, Solid Oxide Fuel Cell Stack Simulation and Optimization, Including Experimental Validation and Transient Behavior, Ph.D. thesis, Lausanne, 3275 pp.
- [58] M. Bram, S. Reckers, P. Drinovac, J. Mönch, R.W. Steinbrech, H.P. Buchkremer, D. Stöver, *Journal of Power Sources* 138 (2004) 111–119.
- [59] A. Nakajo, F. Mueller, D. McLarty, J. Brouwer, J. Van herle, D. Favrat, *Journal of the Electrochemical Society* 158 (2011) B1329–B1340.
- [60] A. Mai, B. Iwanschitz, R. Denzler, D. Habersack, A. Schuler, in: *Proceedings of the 9th European Fuel Cell Forum*, vol. A706.
- [61] J. Van herle, D. Perednis, K. Nakamura, S. Diethelm, M. Zahid, A. Aslanides, T. Somekawa, Y. Baba, K. Horiuchi, Y. Matsuzaki, M. Yoshimoto, O. Bucheli, *Journal of Power Sources* 182 (2008) 389–399.
- [62] ThyssenKrupp, Material data sheet no. 4046.